Materials Research Letters

ISSN: 2166-3831 (Online) Journal homepage: www.tandfonline.com/journals/tmrl20

Enhanced mechanical properties and deformation mechanisms in DED Inconel 625 via printing path switching

J.Y. Li, Jiajia Shen, S.Y. Yuan, W. Dong, Y. Cheng, Y.H. Zhao, J.P. Oliveira, Y. Zhang & K.H. Wang

To cite this article: J.Y. Li, Jiajia Shen, S.Y. Yuan, W. Dong, Y. Cheng, Y.H. Zhao, J.P. Oliveira, Y. Zhang & K.H. Wang (2025) Enhanced mechanical properties and deformation mechanisms in DED Inconel 625 via printing path switching, Materials Research Letters, 13:5, 523-532, DOI: 10.1080/21663831.2025.2476174

To link to this article: https://doi.org/10.1080/21663831.2025.2476174

MATER. RES. LETT.
2025, VOL. 13, NO. 5, 523–532
https://doi.org/10.1080/21663831.2025.2476174

MATERIALS RESEARCH LETTERS
Taylor & Francis
Taylor & Francis Group

ORIGINAL REPORT

Enhanced mechanical properties and deformation mechanisms in DED Inconel 625 via printing path switching

J.Y. Li[a,b*], Jiajia Shen[c*], S.Y. Yuan[a,b], W. Dong[d], Y. Cheng[d], Y.H. Zhao[b,e,f], J.P. Oliveira[c], Y. Zhang[a,b] and K.H. Wang[b,g]

[a]Herbert Gleiter Institute of Nanoscience, Nanjing University of Science and Technology, Nanjing, People's Republic of China; [b]School of Materials Science and Engineering, Nanjing University of Science and Technology, Nanjing, People's Republic of China; [c]CENIMAT/I3N, Department of Materials Science, NOVA School of Science and Technology, Universidade NOVA de Lisboa, Caparica, Portugal; [d]Nanjing Enigma Automation Corporation, LTD, Nanjing, People's Republic of China; [e]Nano and Heterogeneous Materials Center, Nanjing University of Science and Technology, Nanjing, People's Republic of China; [f]School of Materials Science and Engineering, Hohai University, Changzhou, People's Republic of China; [g]The Key Laboratory of Controlled Arc Intelligent Additive Technology Ministry of Industry and Information Technology, Nanjing University of Science and Technology, Nanjing, People's Republic of China

ABSTRACT

In this work, the effects of printing path switching (0° and 90°) at high linear energy density on the grain structure transition and mechanical properties of directed energy deposition-arc (DED-Arc) Inconel 625 alloys were explored. Microstructural analysis on the DED-Arc 625 with near-equiaxed grains under tensile loading revealed that the deformation initially occurs through planar dislocation glide, followed by the formation of dislocation walls and 'locking-clamping' structures, which contribute to strain hardening. The interlayer interfaces did not induce adverse effects on mechanical performance. Additionally, the near-equiaxed grain structure maintained superior mechanical properties at elevated temperatures up to 700 °C.

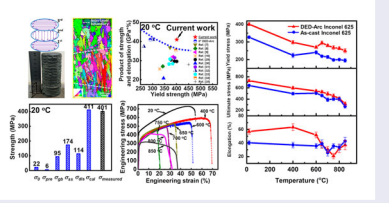

IMPACT STATEMENT

This work explores the impact of printing path switching on the grain structure transition and mechanical properties of Inconel 625 alloy manufactured by DED-Arc. The deformation mechanisms and the influence of layer interfaces on the performance of DED-Arc Inconel 625 with near-equiaxed grains were examined and the high temperature performance of the fabricated components was evaluated.

ARTICLE HISTORY
Received 30 September 2024

KEYWORDS
Additive manufacturing; strain hardening; deformation mechanisms; high temperature performance; near-equiaxed grains

1. Introduction

Among the various additive manufacturing (AM) technologies, directed energy deposition using electric arc (DED-Arc), has gained significant attention for its short manufacturing cycle, high material utilization efficiency, and capability to fabricate large-scale complex structures [1–6]. In recent years, Inconel 625 manufactured via DED-Arc has emerged as an optimal choice for numerous high-temperature and extreme applications due to its exceptional mechanical properties [7–10]. However,

CONTACT Y.H. Zhao yhzhao@njust.edu.cn School of Materials Science and Engineering, Nanjing University of Science and Technology, Nanjing 210094, People's Republic of China, Nano and Heterogeneous Materials Center, Nanjing University of Science and Technology, Nanjing 210094, People's Republic of China School of Materials Science and Engineering, Hohai University, Changzhou 213200, People's Republic of China; J.P. Oliveira jp.oliveira@fct.unl.pt CENIMAT/I3N, Department of Materials Science, NOVA School of Science and Technology, Universidade NOVA de Lisboa, 2829-516 Caparica, Portugal; Y. Zhang yong@njust.edu.cn Herbert Gleiter Institute of Nanoscience, Nanjing University of Science and Technology, Nanjing 210094, People's Republic of China, School of Materials Science and Engineering, Nanjing University of Science and Technology, Nanjing 210094, People's Republic of China; K.H. Wang wkh1602@126.com School of Materials Science and Engineering, Nanjing University of Science and Technology, Nanjing 210094, People's Republic of China, The Key Laboratory of Controlled Arc Intelligent Additive Technology Ministry of Industry and Information Technology, Nanjing University of Science and Technology, Nanjing 210094, People's Republic of China

*These authors contributed equally to this work.

Supplemental data for this article can be accessed online at https://doi.org/10.1080/21663831.2025.2476174.

the typical microstructure of DED-Arc alloys, characterized by a strong $<001>$ oriented columnar grain structure, presents challenges to their mechanical performance, particularly in achieving an optimal balance between strength and ductility [2,5,6]. To address this issue, Li et al. [11] demonstrated that increasing the electric current and, and thereby raising the linear energy density (LED), can effectively facilitate the transition of the grain microstructure into a near-equiaxed structure. This microstructure evolution enhances the material's strength while causing only a marginal reduction in ductility. Consequently, compared to its columnar-grained counterpart, the DED-Arc Inconel 625 alloy with a near-equiaxed grain structure exhibits supervisor overall mechanical performance. Nevertheless, despite these advantages, several critical issues remain unresolved. First, the influence of printing path switching on grain microstructure evolution is not yet fully understood. Studies [12–15] have indicated that interlayer rotation can facilitate the transition from columnar to equiaxed grains. However, these investigations primarily focus on the laser powder bed fusion (LPBF) [12–15] process, with an emphasis on how interlayer rotation influences the initial microstructure and mechanical properties, while paying limited attention to DED-Arc. Second, as a low stacking fault energy (SFE) alloy, Inconel 625 may undergo planar dislocation slip and deformation twining, both of which contribute to strain hardening during plastic deformation [16–19]. However, in the near-equiaxed grain structure of DED-Arc Inconel 625, the predominant deformation mechanism responsible for enhancing strength while only slightly reducing ductility remains unclear.

Furthermore, the unique interlayer interface characteristics inherent to additive manufacturing significantly influence the mechanical properties of Inconel 625, yet this aspect remains underexplored [20–24]. Earlier investigations [20–23] have suggested that the microstructural differences between the interlayer interface and the intralayer may lead to the localized strain accumulation at the interface, potentially causing premature failure at the interface. This effect may be even more pronounced at elevated temperatures, where interlayer interfaces could have a greater impact on deformation uniformity and overall mechanical performance. Therefore, a comprehensive understanding of the influence of interlayer interfaces on the mechanical properties of DED-Arc Inconel 625, particularly under both ambient and high-temperature conditions, is of critical importance. To further expand the application of DED-Arc Inconel 625 in high-temperatures, a comprehensive and in-depth evaluation of its high-temperature mechanical properties is essential. Such an investigation will provide valuable theoretical insights and practical guidance for optimizing DED-Arc processing parameters and enhancing the overall mechanical performance of Inconel 625.

2. Materials and methods

Cold metal transfer (CMT) based on the electric arc was utilized as a heat source to deposit the NiCrMo (Inconel 625) wire with a diameter of 1.2 mm under a gas protection of 70% Ar + 30% He. The spacing between passes in the inner region was 3 mm, with an offset of 3 mm from the contour to the inner region. The trim length for the present DED-Arc processing was 15 mm. After depositing each layer, the welding gun was lifted by 2.5 mm. To ensure stable arc ignition, the electric voltage was initially set to 14 V during the first layer of printing. However, in subsequent layers, the voltage stabilized at 13.4 V. Previous research [11] has shown that to minimize parameter interactions, the electric current should be the sole variable used to adjust the LED. In this study, the electric current, travel speed, and wire feed speed were set to 116 A, 0.6, and 4.6 m/min, respectively, resulting in a calculated LED of 140 J/mm. Here, it is worth mentioning that the first printed layer was excluded from the structural characterization and mechanical testing to eliminate the influence of unstable voltage on the results. For each layer, an outer contour with a thickness of 2.5 mm was initially printed, as illustrated in Figure 1(a). The printing directions for internal deposition on odd and even layers were rotated by 90°, designated as the X-axis and Y-axis, respectively (see Figure 1(b)). Ultimately, a cylinder with a diameter of 50 mm and a length of 100 mm was fabricated, as shown in Figure 1(c). Additionally, the same processing parameters were used to fabricate the 0° DED-Arc 625 alloy, where the subsequent layers are not rotated, allowing for a direct comparison of the effect of printing path switching (0°/90°). After deposition, samples in the Y-Z plane were extracted using electrical discharge machining (EDM) for microstructure and mechanical characterization. To observe the as-deposited microstructures, all samples were initially mechanically polished with SiC sandpapers, followed by 0.5 μm diamond paste. Then, electro-polishing was performed at room temperature using a 10% $HClO_4$ solution at 14 V for 30 s. The X-Ray Diffraction (XRD) was conducted using Cu radiation at 40 kV and 40 mA. For optical microscopy (OM) observations, polished samples were etched for 30 s in an etchant composed of 15 ml CH_3COOH, 10 ml HCl, and 10 ml HNO_3. The OM observations were characterized by a Leica CTR6 optical microscope. The microstructure and elemental distribution were examined using a Carl Zeiss AG scanning electron microscope (SEM), equipped with Electron

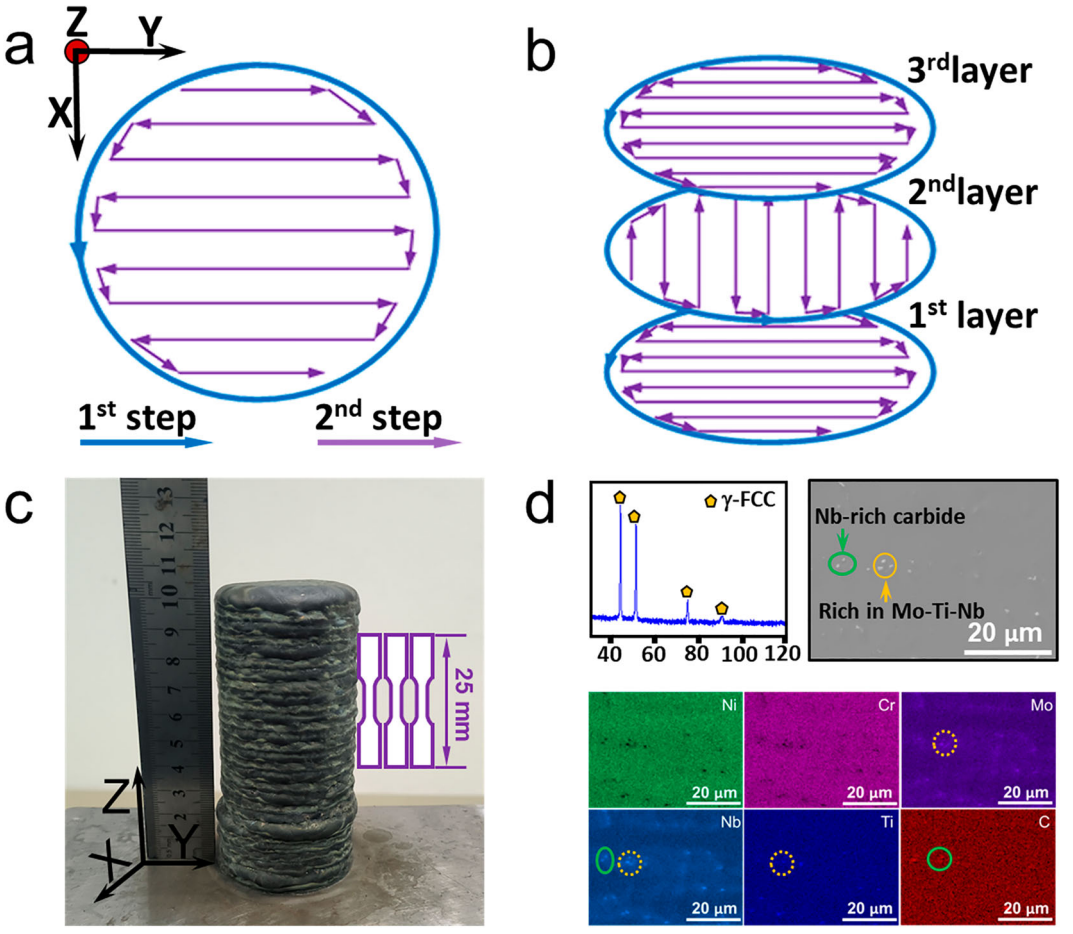

Figure 1. (a,b) Process of DED-Arc. The *Z*-direction is the building direction (BD), and the arrows indicate the movement of the arc; (c) As-fabricated sample with substrate. (d) X-ray diffraction and compositional analysis (local SEM morphology and elemental distribution maps).

Backscatter Diffraction (EBSD) and Energy Dispersive Spectroscopy (EDS) units (with the spot size of 50 nm). EBSD data was processed using MATLAB MTEX, HKL Channel 5 and Image J software. To ensure statistical reliability, more than 200 grains were analyzed. For the Kernel Average Misorientation (KAM), the 2nd neighbor rank, corresponding to a step size of 700 nm, is suitable to obtain information. Transmission electron microscopy (TEM) foils (in the middle of the tensile specimen) with electron transparent area were prepared by electropolishing in a Struers Tenupol-5 unit, using an electrolyte consisting of 100 ml $HClO_4$ and 900 ml Ethyl alcohol at a voltage of 20.5 V and a temperature of −25 °C. TEM observations were performed using a FEI Tecnai 20 microscope operated at 200 kV.

Microhardness tests were conducted using a Qness Q10A + Vickers microhardness tester, applying a 200 g load for 10 s. Microhardness measurements were performed at five different locations and at the same depth to enhance the accuracy and consistency. Tensile tests were carried out on an Instron 5982 tensile machine with a strain rate of 3×10^{-4} s^{-1}. A Digital Image Correlation (DIC) system was used for precise strain measurement. Tensile testing was repeated at least three times for each sample to verify the repeatability of mechanical property measurements. As illustrated in Figure 1(c), all dog-bone-shaped specimens with a gauge section of 5 mm (length) × 2 mm (width) × 1.2 mm (thickness) for testing at room temperature were cut from the *Y*-*Z* plane using Electrical Discharge Machining (EDM), with the tensile axis (TA) aligned parallel to the build direction (BD). Each rod-shaped tensile specimen had a gauge length of 30 mm and a diameter of 5 mm, and tests were conducted at seven different temperatures (400, 600, 650, 700, 750, 800, and 850 °C). The as-cast Inconel 625 alloy was also subjected to high-temperature tensile testing under the same conditions for comparison. The samples were heated to the target temperature at a rate of 6 °C/min and held at that temperature for 30 mins before loading was imposed.

3. Results and discussion

3.1. Microstructure characterization

The XRD pattern of Figure 1(d) depicts that the printed Inconel 625 sample with 90° printing path switching exhibits a face-centered cubic structure, with no detectable secondary phases such as carbides. However, the EDS map reveals the presence of niobium- and titanium-rich precipitates, with an average radius of approximately 0.8 μm and volume fraction of 0.66%. The discrepancy between XRD and EDS results for the precipitates could be attributed to the limited resolution of laboratorial XRD sources [11,25]. In contrast to the columnar grain structure observed in the 0° DED-Arc Inconel 625 (as is shown in Figure S1), which exhibits a strong $<001>$ orientation (similar to other reports on DED-Arc alloys [2,5,6]), the 90° DED-Arc sample (refer to Figure 2(a)) shows intersection angles between the columnar dendrites and the deposition direction. The growth direction of dendrites is governed by the maximum temperature gradient, which does not always align with the deposition direction [25,26]. Figure 2(b–d) present a detailed view of the 90° DED-Arc microstructure. Due to heterogeneous nucleation and uneven heat dissipation at the boundary of the molten pool [25], a fine isotropic dendrite structure forms at the layer boundaries. Figure 2(e) illustrates a grain structure, with an average length of 527 ± 5 μm and a width of 172 ± 7 μm (obtained through Image J software) according to the high angle grain boundaries (HAGBs, $> 15°$), giving a grain aspect ratio of approximately 3.06. The sample is characterized by near-equiaxed grain features. Furthermore, a fine-grained structure with an average grain size of 37 ± 2 μm, comprising approximately $\sim 3.4\%$ of the material, is observed at the layer boundaries. These grains are notably smaller than these located away from the boundaries, which have an average grain size of 232 ± 16 μm, as determined by equivalent diameter through EBSD analysis. Additionally, the corresponding inverse pole figures (IPFs) for the *X*, *Y* and *Z* axis are shown in Figure 2(e). In the *Z*-axis (parallel to tensile axis, TA), a relatively random orientation is observed. Based on high LED, printing path switching promotes the formation of a near-equiaxed grain microstructure. It is important to note that under low LED conditions, the effect of printing path switching is limited, as it does not facilitate the transition from columnar to near-equiaxed grains [11]. As a result, the columnar grain growth tendency is maintained, while formation of equiaxed grains is suppressed. This finding underscores the importance of combining high LED conditions with printing path switching for promoting the grain structure transition from columnar to near-equiaxed grains. Under high LED conditions, the temperature gradient in the melt pool can be significantly reduced, weakening thermal convection effects and creating a more favorable environment for equiaxed grain nucleation and growth. Additionally, high LED may increase the depth of the remelted layer. While this adds complexity to the thermal cycle, it also provides more opportunity for recrystallization, contributing to grain refinement. Meanwhile, under high LED conditions, printing path switching becomes more effective in disrupting the growth of epitaxial grains. This disruption not only provides new nucleation sites for grain formation but also promotes the development of more equiaxed grain nuclei within the melt pool. These nuclei then grow into equiaxed grains, thereby altering the overall grain structure of the material. In conclusion, controlling the grain structure in additive manufacturing requires the combined influence of high LED and printing path switching. High LED creates favorable conditions for the nucleation and growth of equiaxed grains, while printing path switching helps disrupt epitaxial grain growth and promote equiaxed grain nucleation within the melt pool. Therefore, implementing a printing path switching under high LED conditions is an effective strategy to facilitate the transition from columnar to near-equiaxed grains, thereby optimizing the material's microstructure and properties.

3.2. Mechanical response at room temperature

As shown in Figure 3(a_1), the near-equiaxed sample exhibits high yield strength ($\sim 401 \pm 12$ MPa), ultimate tensile strength ($\sim 724 \pm 5$ MPa), and tensile elongation ($\sim 57 \pm 5\%$). Although the elongation of the 90° DED-Arc Inconel 625 is slightly lower than that of the 0° DED-Arc Inconel 625 ($\sim 66 \pm 4\%$), reflecting a reduction of $\sim 9\%$, its advantage in strength is particularly notable. The yield strength and ultimate tensile strength of the 90° are significantly higher than those of the 0° sample, which are 291 ± 8 and 621 ± 8 MPa (Figure S1c), respectively, representing an increase of approximately 110 and 103 MPa. Notably, a slight concavity observed in the true stress–strain curve within the true strain range of 8–25% indicates the occurrence of secondary strain hardening in this strain range [11]. Figure 3(a_2) reveals the dynamic relationship between true strain and work hardening rate, showcasing a typical three-stage strain hardening behavior that is common in alloys with low SFE [27,28]. In stage A (5–8% true strain), the work hardening rate undergoes a continuous decrease, approaching *G*/50 (where *G* is the shear modulus, 78 GPa), reflecting the rapid plastic deformation and dislocation accumulation experienced by the material during the onset of loading. Then, in stage B (8–25% true strain), the work hardening

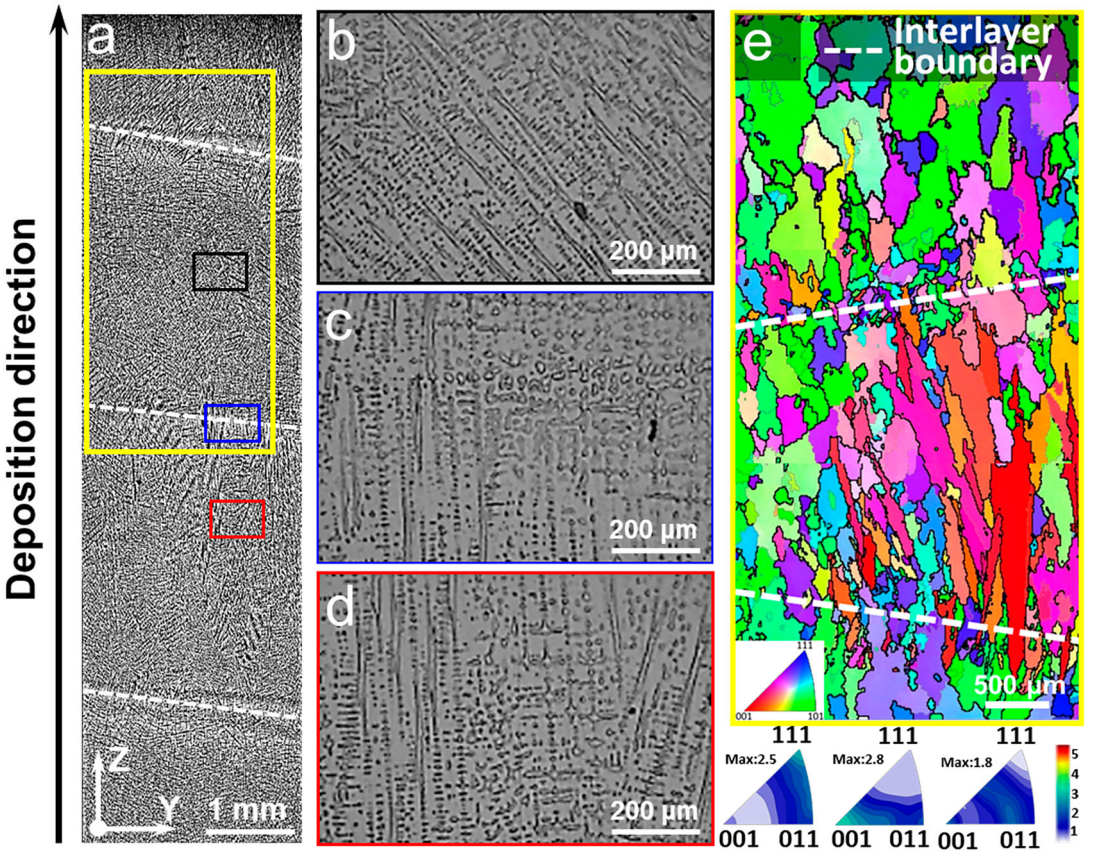

Figure 2. Optical microscopy image of the as-deposited sample: (a) macrostructure and (b–d) detailed microstructure of dendrites and layer boundaries. (e) EBSD orientation map of plane *YOZ*. The black lines represent high angle grain boundaries (HAGBs, > 15°) and the grey lines represent low angle grain boundaries (LAGBs, 2–15°). The color code is IPF coloring-*Z* inserted at the lower left corner; and at the bottom, crystallographic texture obtained on the *X, Y* and *Z* axis, respectively.

rate experiences a gradual recover, reaching approximately 1880MPa (*G*/40), indicating the occurrence of secondary strain hardening. Ultimately, in stage C, as the material approaches fracture, the work hardening rate gradually decreases. Furthermore, combined with its high tensile strength and ductility, the sample exhibits an exceptionally high tensile strength-ductility product (∼41.3 GPa∗%) and a yield strength (∼401 MPa) that far exceeds that of 0° DED-Arc Inconel 625 sample and other Inconel 625 alloys prepared by DED-Arc reported in the literature (see Figure 3(a_3) [7–10,29–35]. Moreover, when compared to commercially available hot-rolled Inconel 625 alloy, which boasts a yield strength of 348 MPa and a tensile strength-ductility product of 32.1 GPa∗% [36], the near-equiaxed sample undoubtedly demonstrates a superior combination of strength and ductility at room temperature.

Interestingly, the near-equiaxed sample exhibits an average grain size of 232 ± 16 μm (with a similar equivalent diameter obtained through EBSD processing), and its yield strength exceeds 400 MPa, significantly higher than that of the standard hot-rolled Inconel 625 sample with smaller grain sizes (< 130 μm) [36]. To elucidate the reason behind the high yield strength of the near-equiaxed sample, the contributions of various strengthening mechanisms were calculated. The primary strengthening mechanisms in metallic alloys include solid solution strengthening (σ_{ss}), dislocation strengthening (σ_{dis}), grain boundary strengthening (σ_{gb}), and precipitation strengthening (σ_{pre}). Therefore, the total contribution to yield strength can be expressed as in Eq. (1), and the detailed calculations are provided in the Supplementary materials appended to the paper:

$$\sigma_{cal} = \sigma_0 + \sigma_{pre} + \sigma_{gb} + \sigma_{ss} + \sigma_{dis} \quad (1)$$

where σ_0 represents the friction stress. Figure 3(b_4) presents the calculated contributions of each strengthening mechanism, with grain boundary strengthening (σ_{gb}), solid solution strengthening (σ_{ss}), and dislocation strengthening (σ_{dis}) contributions, these being ∼95, ∼174, and ∼114 MPa, respectively. The calculated total yield strength of the near-equiaxed grain sample is ∼411 MPa, which aligns well with the experimental result (411

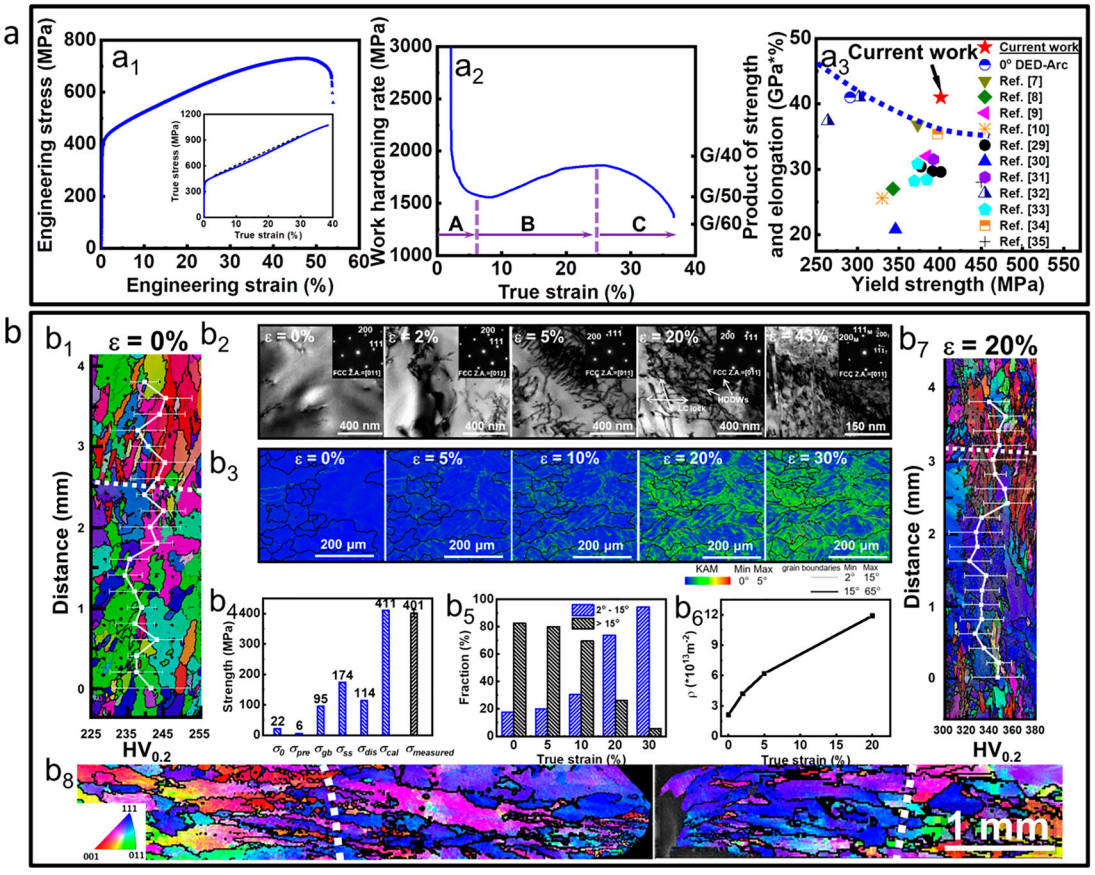

Figure 3. (a) Mechanical properties: (a_1) tensile stress-strain curves. (a_2) Work hardening rate versus true strain. (a_3) yield strength versus the PSE compared with another reported DED-Arc Inconel 625 [7–10,29–35]. (b) Deformation structures evolution: (b_1) EBSD orientation map overlaid with the longitudinal microhardness (average with standard deviation). (b_2) TEM micrograph with corresponding SAED pattern ([011] zone axis insets). (b_3) Kernel average misorientation (KAM) data of the representative structures. Blue, green and red colors in the rainbow bar represent low ($<$ 1°), medium (from 1° to 3°) and high (from 3° to 5°) misorientations, respectively. (b_4) Calculated contributions of each strengthening mechanism. (b_5) Distribution of grain boundaries and (b_6) dislocation density at different true strains. (b_7) EBSD orientation map and the average longitudinal microhardness with standard deviation at 20% true strain. (b_8) Fracture and evolution of deformation structures: Orientation map of *YOZ* plane at the fracture. Layer-to-layer interfaces are marked with white lines.

vs. 401 MPa). Given that the composition of the DED-processed 625 sample is similar to that of the hot-rolled 625 sample [36], the effect of solid solution strengthening on the yield strength is nearly identical. While grain boundary strengthening contributes $\sim$112 MPa, this contribution is relatively modest compared to the hot-rolled Inconel 625 samples with smaller grain sizes [36]. Thus, it can be concluded that dislocation strengthening is the primary factor driving the superior strength performance of the near-equiaxed grain sample.

To explore the underlying mechanisms responsible for the superior work hardening and tensile ductility of the near-equiaxed samples, the dynamic evolutions of microhardness and deformation substructures at different strains with EBSD and TEM were investigated carefully. Prior to tensile loading, the microhardness along the building direction (Figure 3(b_1)) does not exhibit significant changes at the layer interfaces, maintaining an average hardness of $\sim 240 \pm 7$ $HV_{0.2}$. Even when the sample is deformed to 20% (Figure 3(b_7)), though the average hardness is significantly promoted to $\sim 335 \pm 24$ $HV_{0.2}$ due to the strong strain hardening, the fluctuations of the hardness at various locations are still quite similar to those in the undeformed sample. No drastic changes on the hardness around the interface are detected. As shown in Figure 3(b_8), the orientation map of the fracture surfaces reveals similar structural features, indicating that the fracture occurs within the grain, consistent with a typical transgranular fracture mode. Furthermore, at the strain of $\sim$57%, the printing layer should theoretically elongated to approximately $\sim$4 mm, which aligns well with the measured distance between the fracture surfaces and the layer interfaces ($\sim$2.03 and $\sim$2.42 mm). This confirms that fracture occurred in the middle of the intralayer (a more detailed analysis is available in the Supplementary materials). This indicates that the

microstructural differences in the grains at these interfaces do not adversely affect the mechanical properties. These results indicate that the introduction of interface by the printing path switching during DED-Arc does not induce localized plastic deformation detrimental to the sustained work hardening capabilities.

Considering the deformation mechanisms, Inconel 625 alloy exhibits intricate dislocation evolutions during tensile testing. Before loading, pre-existing dislocation structures arises due to thermal distortions during printing influenced by melt pool constraints and thermal cycling [37–39]. This results in a higher initial dislocation density compared to conventionally manufactured materials [37–39]. In stage A (initial deformation, true strain below 8%, Figure 3(a_2)), high-density dislocation walls (HDDWs) dominate the microstructure in the strained sample (Figure 3(b_2)), a characteristic of low SFE alloy [16–19]. With increasing strain (8–25% true strain at the secondary strain hardening stage), dislocation activity intensifies on conjugate 111 slip planes, leading to the formation of Lomer-Cottrell (L-C) locks at slip band intersections. TEM analysis on the microstructure at the secondary strain hardening stage indicates that the microstructural features are dominated by the dense planar dislocation structures containing high densities of L-C locks and intensive HDDWs on various 111 planes. These can act as effective dislocation barriers, significantly increasing internal stress and thereby enhancing strain hardening, corresponding to the work hardening rising (stage B) seen in Figure 3(a_2). Figure 3(b_3) shows that with increasing tensile strain, enhanced KAM values are frequently observed along slip bands, corresponding to the HDDW structures identified in TEM [16]. Figure 3(b_5) further displays that high density of low-angle grain boundaries appear with medium strains, which indicates the formation of high density HDDWs. As shown in Figure 3(b_6), the defect density (the detailed calculations are provided in the Supplementary materials) increases by ~6 times in the strain range of 0–20%. The rapid accumulation of dislocation density may lead to a slight decrease in ductility and a significant increase in strength. Notably, even at strains approaching 43% (Figure 3(b_2)), the Inconel 625 alloy does not exhibit significant deformation twinning. Instead, the combined use of TEM and EBSD analysis reveals that deformation in the current near-equiaxed samples is primarily controlled by dislocation slip, with single slip mechanisms dominating in the initial stages of tensile deformation. As strain reaches 20%, planar dislocation substructures further develop on conjugate 111 slip planes, resulting in a

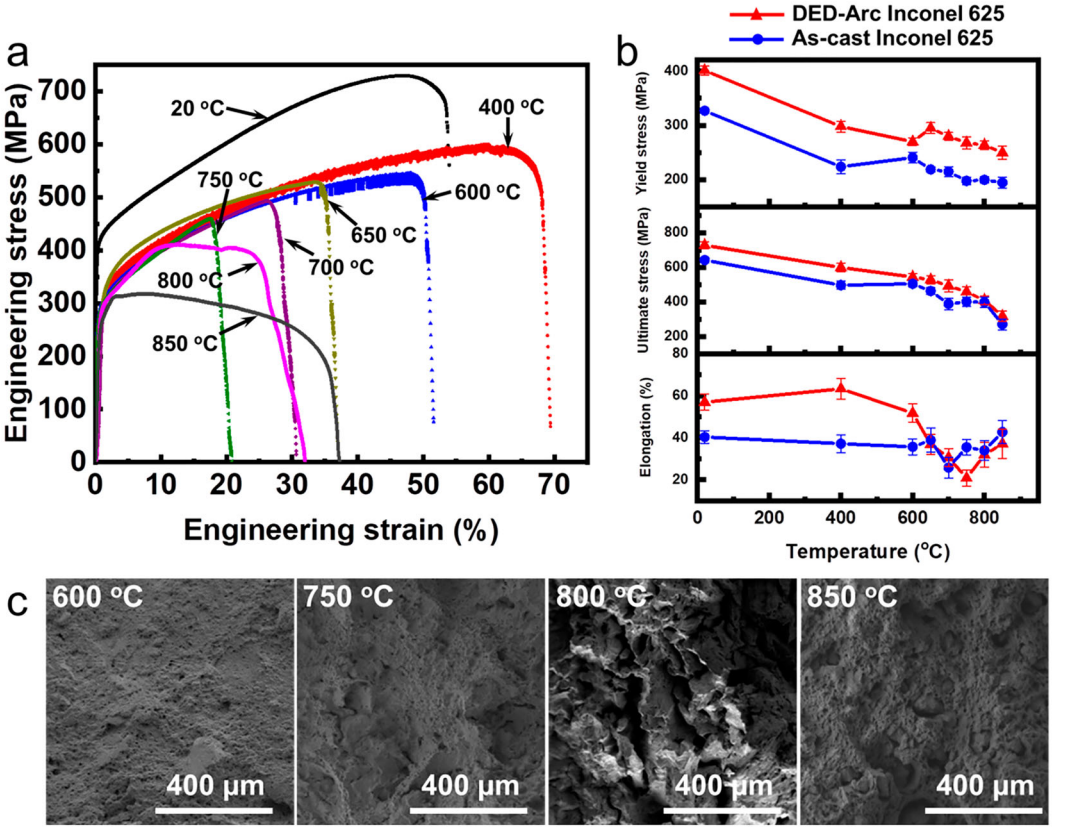

Figure 4. (a) Tensile curves along the deposition direction. (b) Yield stress, ultimate tensile stress and elongation comparison of DED-Arc and as-cast Inconel 625 at different temperatures. (c) SEM images for fracture surface.

complex network characterized by numerous planar dislocation layers and intense Lomer-Cottrel (L-C) locked dislocation substructures. These L-C locks serve as effective dislocation barriers, significantly elevating the internal stress levels within the deformed material. Overall, the high strength and superior strain hardening capabilities of the DED-produced near-equiaxed sample primarily stems from its pronounced dislocation strengthening effect, complemented by grain boundary strengthening and solid solution strengthening. Additionally, the excellent bonding at interlayer interfaces ensures the overall structural stability and sustains mechanical performance of the material during tensile testing.

3.3. Mechanical response at elevated temperatures

To investigate the mechanical response of the near-equiaxed Inconel 625 sample at elevated temperatures, Figure 4(a) presents the engineering stress–strain curves of the samples under different temperatures, while Figure 4(b) further reveals the dependence of yield strength, ultimate strength, and elongation on temperature, comparing these results with the mechanical properties of cast Inconel 625. In terms of strength, the near-equiaxed Inconel 625 samples exhibit significantly higher values compared to the cast samples. In what concerns ductility, at temperatures below 700 °C, the elongation of the near-equiaxed Inconel 625 is higher than that of casting samples; however, at temperatures above 700 °C, the elongation is slightly lower. Figure 4(c) shows the fracture morphology after high-temperature tensile testing. At a testing temperature of 600 °C, the fracture morphology exhibits typical trans-granular ductile fracture features, with shallow dimples spread across the fracture surface, indicating a ductile fracture mode [3]. However, as the testing temperature increases to 750 and 800 °C, the crack propagation mode changes significantly, shifting to intergranular fracture with the appearance of brittle facets, indicating that the material gradually loses its ductility. When the temperature further rises to 850 °C, the fracture surface becomes more complex, with numerous uneven dimples coexisting with a few brittle fracture areas, suggesting a mixed fracture mode of both ductile and brittle characteristics under these conditions. The fracture mechanism affecting the mechanical performance at high temperatures will be further investigated in future work.

4. Conclusions

This work highlights the influence of printing path switching on the transition from coarse columnar grains to near-equiaxed grains and its effect on the mechanical properties. Under high LED, 90° printing path switching promotes the formation of a near-equiaxed grain microstructure. EBSD and TEM analysis are combined to reveal that the tensile deformation is accommodated through a complex dislocation evolution process, involving planar dislocation glide, the formation of high-density dislocation walls, and the emergence of 'locking-clamping' dislocation structures. The synergistic effects of these mechanisms significantly enhance the strain-hardening capacity of the material, contributing to its excellent ductility. Additionally, the presence of fine grains at the layer interfaces contributes to enhanced mechanical properties at these regions, further dispelling concerns regarding any detrimental effects of layer interfaces on the mechanical properties. Furthermore, the DED-Arc Inconel 625 alloy with a near-equiaxed grain microstructure exhibits superior mechanical performance at both room and evaluated temperatures, reinforcing its potential for superalloy manufacturing.

Disclosure statement

No potential conflict of interest was reported by the author(s).

Funding

This work was supported by the National Natural Science Foundation of China (51601091), the Jiangsu Province Leading Edge Technology Basic Research Major Project (BK 20222014), the Natural Science Foundation of Jiangsu Province (BK 20160826), the Six Talent Peaks Project of Jiangsu Province (2017-XCL-051), the Fundamental Research Funds for the Central Universities (30917011106), the Key Research and Development Plan of Jiangsu Province (BE 2020085) and the Jiangsu Funding Program for Excellent Postdoctoral Talent (2024ZB653). JS and JPO acknowledge the financial support provided by Fundação para a Ciência e a Tecnologia (FCT – MCTES) under the projects UID/00667/2020 (UNIDEMI), LA/P/0037/2020, UIDP/50025/2020 and UIDB/50025/2020. JS acknowledge to the China Scholarship Council for funding their Ph.D. studies (CSC NO. 201808320394).

References

[1] Yang ZW, Liu Q, Wang Y, et al. Fabrication of multi-element alloys by twin wire arc additive manufacturing combined with in-situ alloying. Mater Res Lett. 2020;8(12):477–482.

[2] Xu XF, Ganguly S, Ding JL, et al. Improving mechanical properties of wire plus arc additively manufactured maraging steel through plastic deformation enhanced aging response. Mater Sci Eng A – Struct Mater Propert Microstruct Process. 2019;747:111–118.

[3] Farias FWC, Duarte VR, Payao JD, et al. Arc-based directed energy deposited Inconel 718: role of heat treatments on high-temperature tensile behavior. Mater Res Lett. 2024;12(2):97–107.

[4] Squires L, Roberts E, Bandyopadhyay A. Radial bimetallic structures via wire arc directed energy deposition-based additive manufacturing. Nat Commun. 2023;14(1). https://www.nature.com/articles/s41467-023-39230-w#article-info
[5] Caballero A, Davis AE, Kennedy JR, et al. Microstructural characterisation and mechanical properties of Ti-5Al-5V-5Mo-3Cr built by wire and arc additive manufacture. Philos Mag. 2022;102(22):2256–2281.
[6] Kennedy JR, Davis AE, Caballero AE, et al. The potential for grain refinement of wire-arc additive manufactured (WAAM) Ti-6Al-4 V by ZrN and TiN inoculation. Additive Manufacturing. 2021;40:101928.
[7] Tanvir ANM, Ahsan RU, Seo G, et al. Heat treatment effects on Inconel 625 components fabricated by wire plus arc additively manufacturing (WAAM)-part 2: mechanical properties. Int J Adv Manuf Technol. 2020;110(7-8):1709–1721.
[8] Wang JF, Sun QJ, Wang H, et al. Effect of location on microstructure and mechanical properties of additive layer manufactured Inconel 625 using gas tungsten arc welding. Mater Sci Eng A – Struct Mater Prop Microstruct Process. 2016;676:395–405.
[9] Wang YF, Chen XZ, Shen QK, et al. Effect of magnetic field on the microstructure and mechanical properties of inconel 625 superalloy fabricated by wire arc additive manufacturing. J Manuf Process. 2021;64:10–19.
[10] Raja M, Tiwari Y, Mukherjee M, et al. Effect of bidirectional and switchback deposition strategies on microstructure and mechanical properties of wire arc additive manufactured Inconel 625. Int J Adv Manuf Technol. 2022;119(7-8):4845–4861.
[11] Li S, Li JY, Jiang Z, et al. Controlling the columnar-to-equiaxed transition during directed energy deposition of Inconel 625. Addit Manuf. 2022;57:102958.
[12] Xi X, Lin DY, Song XG, et al. In-situ remelting induced healing of cracks and strength-ductility synergy in additively manufactured Haynes 230 alloy. Addit Manuf. 2025;98:104638.
[13] He J, Hu YQ, Luo ZR, et al. The influence of rotation angle between layers in laser-based powder bed fusion on the hydrogen embrittlement of Ni. J Mater Res Technol-Jmr&T. 2023;23:3187–3195.
[14] Zhao JM, Sun LY, Ji PG, et al. The effect of scanning strategies on the microstructure and mechanical properties of M2052 alloy manufactured by selective laser melting. J Mater Res Technol-Jmr&T. 2023;27:7084–7093.
[15] Gupta MK, Singla AK, Ji HS, et al. Impact of layer rotation on micro-structure, grain size, surface integrity and mechanical behaviour of SLM Al-Si-10Mg alloy. J Mater Res Technol-Jmr&T. 2020;9(5):9506–9522.
[16] Gutierrez-Urrutia I, Raabe D. Dislocation and twin substructure evolution during strain hardening of an Fe-22 wt.% Mn-0.6 wt.% C TWIP steel observed by electron channeling contrast imaging. Acta Mater. 2011;59(16):6449–6462.
[17] Gutierrez-Urrutia I, Zaefferer S, Raabe D. The effect of grain size and grain orientation on deformation twinning in a Fe-22 wt.% Mn-0.6 wt.% C TWIP steel. Mater Sci Eng A – Struct Mater Prop Microstruct Process. 2010;527(15):3552–3560.
[18] Canadinc D, Sehitoglu H, Maier HJ, et al. Strain hardening behavior of aluminum alloyed Hadfield steel single crystals. Acta Mater. 2005;53(6):1831–1842.
[19] Canadinc D, Sehitoglu H, Maier HJ. The role of dense dislocation walls on the deformation response of aluminum alloyed Hadfield steel polycrystals. Mater Sci Eng A – Struct Mater Prop Microstruct Process. 2007;454:662–666.
[20] Vishnukumar M, Muthupandi V, Jerome S. Microstructural characteristics, mechanical properties and corrosion performance of super austenitic stainless steel 904L produced by wire arc additive manufacturing. Mater Today Commun. 2023;35:105801.
[21] Kindermann RM, Roya MJ, Moranac R, et al. Wire-arc directed energy deposition of inconel 718: effects of heat input and build interruptions on mechanical performance. J Magnes Alloys. 2023;12:5024–5037.
[22] Xi NY, Tang KX, Fang XW, et al. Enhanced comprehensive properties of directed energy deposited Inconel 718 by a novel integrated deposition strategy. J Mater Sci Technol. 2023;141:42–55.
[23] Yang Y-H, Guan Z-P, Ma P-K, et al. (2023). Wire arc additive manufacturing of a novel ATZM31 Mg alloy: microstructure evolution and mechanical properties.
[24] Xu X, Mi GY, Chen L, et al. Research on microstructures and properties of Inconel 625 coatings obtained by laser cladding with wire. J Alloys Compd. 2017;715:362–373.
[25] Li S, Wei QS, Shi YS, et al. Microstructure characteristics of Inconel 625 superalloy manufactured by selective laser melting (Vol. 31, pp. 946, 2015). J Mater Sci Technol. 2016;32(7):E1–EE.
[26] Thijs L, Sistiaga MLM, Wauthle R, et al. Strong morphological and crystallographic texture and resulting yield strength anisotropy in selective laser melted tantalum. Acta Mater. 2013;61(12):4657–4668.
[27] Hamdi F, Asgari S. Evaluation of the role of deformation twinning in work hardening behavior of face-centered-cubic polycrystals. Metallurg Mater Transact A – Phys Metallurg Mater Sci. 2008;39A(2):294–303.
[28] Asgari S, El-Danaf E, Kalidindi SR, et al. Strain hardening regimes and microstructural evolution during large strain compression of low stacking fault energy fcc alloys that form deformation twins. Metall Mater Trans A, Phys Metall Mater Sci (USA). 1997;28A(9):1781–1795.
[29] Wang YF, Chen XZ, Su CC. Microstructure and mechanical properties of Inconel 625 fabricated by wire-arc additive manufacturing. Surf Coat Technol. 2019;374:116–123.
[30] Wang XL, Hu QX, Li TQ, et al. Microstructure and fracture performance of wire arc additively manufactured Inconel 625 alloy by hot-wire GTAW. Metals (Basel). 2022;12(3):510.
[31] Votruba V, Divis I, Pilsová L, et al. Experimental investigation of CMT discontinuous wire arc additive manufacturing of Inconel 625. Int J Adv Manuf Technol. 2022;122(2):711–727.
[32] Mookara RK, Seman S, Jayaganthan R, et al. Influence of droplet transfer behaviour on the microstructure, mechanical properties and corrosion resistance of wire arc additively manufactured Inconel (IN) 625 components. Weld World. 2021;65(4):573–588.

[33] Kumar SM, Kannan AR, Kumar NP, et al. Microstructural features and mechanical integrity of wire arc additive manufactured SS321/Inconel 625 functionally gradient material. J Mater Eng Perform. 2021;30(8):5692–5703.
[34] James WS, Ganguly S, Pardal G. Selection and performance of AM superalloys for high-speed flight environments. Int J Adv Manuf Technol. 2022;122(5–6):2319–2327.
[35] Guo C, Ying M, Dang HY, et al. Microstructural and intergranular corrosion properties of Inconel 625 superalloys fabricated using wire arc additive manufacturing. Mater Res Express. 2021;8(3):035103.
[36] Gao YB, Ding YT, Ma YJ, et al. Evolution of annealing twins in Inconel 625 alloy during tensile loading. Mater Sci Eng A – Struct Mater Propert Microstruct Process. 2022;831:142188.
[37] Bertsch KM, de Bellefon M, Kuehl G, et al. Origin of dislocation structures in an additively manufactured austenitic stainless steel 316L. Acta Mater. 2020;199:19–33.
[38] Pham MS, Dovgyy B, Hooper PA. Twinning induced plasticity in austenitic stainless steel 316L made by additive manufacturing. Mater Sci Eng A – Struct Mater Prop Microstruct Process. 2017;704:102–111.
[39] Saeidi K, Gao X, Zhong Y, et al. Hardened austenite steel with columnar sub-grain structure formed by laser melting. Mater Sci Eng A – Struct Mater Prop Microstruct Process. 2015;625:221–229.